Collective excitations of the Chern-insulator states in commensurate double moiré superlattices of twisted bilayer graphene on hexagonal boron nitride

Xianqing Lin,[1,*] Quan Zhou,[1] Cheng Li,[1] and Jun Ni[2]
[1]*College of Science, Zhejiang University of Technology, Hangzhou 310023, China*
[2]*State Key Laboratory of Low-Dimensional Quantum Physics and Frontier Science Center for Quantum Information, Department of Physics, Tsinghua University, Beijing 100084, China*

(Received 12 January 2023; revised 26 March 2023; accepted 15 May 2023; published 24 May 2023)

We study the collective excitation modes of the Chern insulator states in magic-angle twisted bilayer graphene aligned with hexagonal boron nitride (TBG/BN) at odd integer fillings (ν) of the flat bands. For the 1×1 commensurate double moiré superlattices in TBG/BN at three twist angles (θ') between BN and graphene, self-consistent Hartree-Fock (HF) calculations show that the electron-electron interaction and the broken C_{2z} symmetry lead to the Chern-insulator ground states with valley-spin flavor polarized HF bands at odd ν. In the active-band approximation, the HF bands in the same flavor of TBG/BN are much more separated than those of the pristine TBG with TBG/BN having a larger intraflavor band gap so that the energies of the lowest intraflavor exciton modes of TBG/BN computed within the time-dependent HF method are much higher than those of TBG and reach about 20 meV and the exciton wave functions of TBG/BN become less localized than those of TBG. The interflavor valley-wave modes in TBG/BN have excitation energies higher than 2.5 meV, which is also much larger than that of TBG, while the spin-wave modes all have zero excitation gap. In contrast to TBG with particle-hole symmetric excitation modes for positive and negative ν, the excitation spectrums and gaps of TBG/BN at positive ν are rather different from those at negative ν. The quantitative behavior of the excitation spectrum of TBG/BN also varies with θ'. Full HF calculations demonstrate that more HF bands besides the two central bands can have rather large contributions from the single-particle flat-band states; then the lowest exciton modes that determine the optical properties of the Chern insulator states in TBG/BN are generally the ones between the remote and flatlike bands, while the valley-wave modes have similar energies as those in the active-band approximation.

DOI: 10.1103/PhysRevB.107.195434

I. INTRODUCTION

Flat bands with vanishing bandwidths and well separated from other remote bands occur around the Fermi level in magic-angle twisted bilayer graphene (TBG) [1–7] and the experimental realization of such TBG intrigued great interest in exploring various electronic, transport, and optical properties associated with the flat bands [8–30]. The emergence of correlated insulator states at integer filling of the flat bands in TBG and the superconductivity in the vicinity of these insulating states have been observed and theoretically comprehended [8–22,24,31–55]. There are eight single-particle flat bands taking into account the spin and valley degrees in TBG; then the electron filling of the flat bands per moiré supercell relative to charge neutrality point (CNP) is in the range of -4 to 4. At odd ν, the ground states are Chern insulators with spontaneously broken symmetry in the valley and spin degrees due to the electron-electron (e-e) interaction [39–41,43,46–48,50,51,55]. The alignment of TBG with BN breaks the C_{2z} symmetry in the relaxed atomic structure and the single-particle Hamiltonian [51,56–61] and thus enhances the energy gaps of such Chern insulator states [39,43,46,51]. In particular, the quantum anomalous Hall effect associated with their finite Chern numbers has been experimentally realized in TBG aligned with BN (TBG/BN) [62,63]. For such insulating correlated states, low-energy collective excitation states may appear within the gap due to the Coulomb interaction between the particle and hole states. In experiments, the observed Pomeranchuk effect from the measured electron compressibility in TBG at extremely low temperatures implies the presence of the low-energy collective excitations for the correlated insulator states [24]. The optical excitations in the infrared regime have also been observed in twisted graphene systems around the integer fillings of the flat bands [23,25,26]. It is also noted that the experimentally observed low-energy response properties of the correlated states in TBG at positive and negative filling factors exhibit particle-hole asymmetry [11,17–19,62,64].

For the pristine TBG or the TBG with a sublattice potential difference [46,53,54,65–67], theoretical analysis or Hartree-Fock (HF) calculations indeed demonstrated the occurrence of the low-energy collective excitation modes of interflavor spin wave, valley wave, and intraflavor exciton at odd ν. The spin-wave excitation states are Goldstone modes with a zero excitation gap [46,53,54,66]. The valley-wave modes have an extremely small excitation gap for the pristine TBG [66] and a sublattice potential difference increases their excitation

*xqlin@zjut.edu.cn

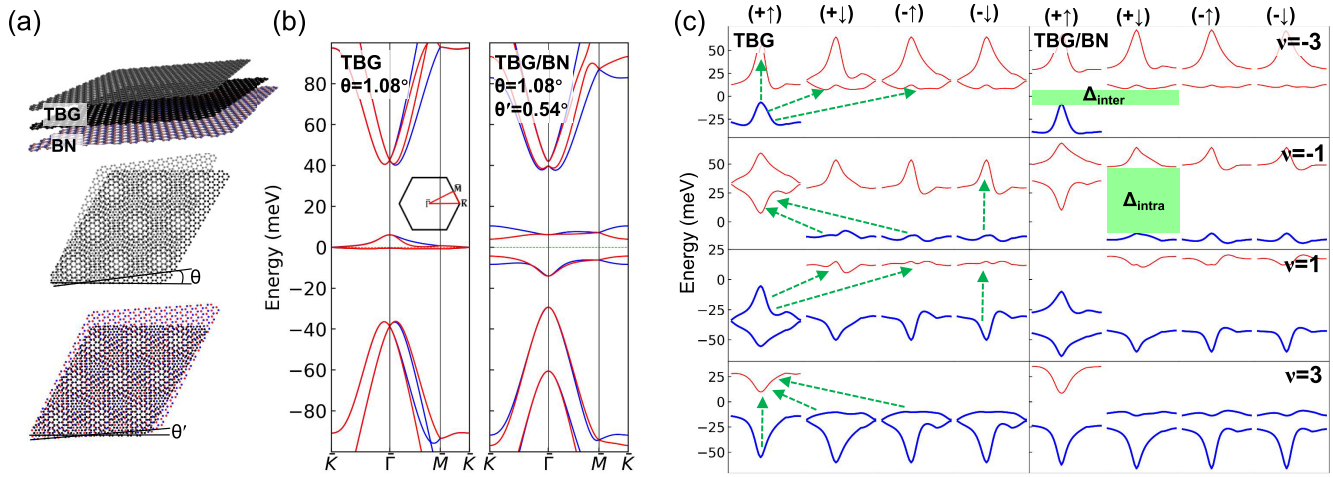

FIG. 1. Single-particle and HF band structures of TBG and TBG/BN. (a) The schematic view of the commensurate double moiré superlattices in TBG/BN. The twist angle (θ) between the graphene layers and that (θ') between graphene and BN are labeled. (b) The single-particle band structures of TBG at the magic $\theta = 1.08^\circ$ and a commensurate supercell of TBG/BN at $\theta' = 0.54^\circ$. The red and blue lines represent bands in the $\xi = +$ valley and the $\xi = -$ valley, respectively. (c) The HF band structures of the Chern-insulator ground states at odd ν in the active-band approximation for the TBG and TBG/BN systems in (b). The HF bands of each flavor are plotted separately along the k-point path same as that in (b) and the flavor is labeled by the valley ($+$ or $-$) and spin ($\uparrow$ or $\downarrow$) indices. The conduction and valence bands are represented by the red and blue lines, respectively. The intraflavor energy gap (Δ_{intra}) between the conduction and valence bands in the same flavor and the interfavor energy gap (Δ_{inter}) between the highest valence band in one flavor and the lowest conduction band in another flavor are labeled by the green shades. The spin-wave excitation between the valence and conduction bands in two different flavors with the same valley index but the opposite spin indices, and the valley-wave excitation between the bands in two flavors with the same spin index but the opposite valley indices, and the exciton excitation between bands in the same flavor are indicated by the dashed green lines.

energies [46]. For the pristine TBG, low energy exciton states of a few meV also appear [66]. We note that all the previous calculations focused on one odd ν of -3 or 3 and adopted the active-band approximation that considers only the excitations between flat bands [46,66]. A full HF calculation of the excitation states at all odd ν may provide more excitation modes and can influence the excitation energy spectrums. For TBG/BN with enhanced Chern insulator states at odd ν, previous studies have established that BN induces not only the sublattice potential difference in graphene but also spatially varying effective moiré potentials and the structural deformation due to the interlayer vdW interaction between BN and graphene also strongly breaks the C_{2z} symmetry of the single-particle Hamiltonian [51,57]. Moreover, the correlated band structure of TBG/BN changes with the twist angle (θ') between TBG and BN [51,56]. Therefore, it is desirable to explore systematically the collective excitation modes at all odd ν for all the possible commensurate configurations of TBG/BN.

Here, we demonstrate that the energies of the lowest intraflavor exciton modes of TBG/BN are much higher than those of TBG and reach about 20 meV, the interflavor valley-wave modes have excitation energies higher than 2.5 meV, which is also much larger than that of TBG, while the spin-wave modes all have zero excitation gap. The excitation spectrums and gaps of TBG/BN at positive ν are rather different from those at negative ν, which contrasts with the particle-hole symmetric excitation modes for positive and negative ν in TBG. Full HF calculations indicate that the lowest exciton modes that determine the optical properties of the Chern insulator states in TBG/BN are generally the ones between the remote and flatlike bands, while the valley-wave modes have similar energies as those in the active-band approximation. Moreover, the quantitative behavior of the excitation spectrum of TBG/BN also varies with θ'.

II. HF BANDS AND EXCITATIONS IN THE ACTIVE-BAND APPROXIMATION

For TBG with the magic twist angle of $\theta = 1.08^\circ$ aligned with BN, we consider the 1×1 commensurate supercells of TBG/BN at three twist angles θ' between BN and its adjacent graphene layer of 1.64°, 0.54°, and -0.56°, as seen in Fig. 1(a), and their structural parameters are detailed in the Appendix. At the origin of the TBG/BN supercell, both the local stackings between the graphene layers and between graphene and BN are taken to be the AA stacking. The moiré superlattices of TBG/BN and the pristine TBG are fully relaxed based on the continuum elastic theory to obtain their stable atomic structures [51,57].

For the fully relaxed TBG/BN, an effective single-particle tight-binding model (H^0) of the graphene layers can be built taking into account the relaxation effect and the full moiré Hamiltonian induced by BN; the on-site energies and hopping terms of the tight-binding Hamiltonian within a moiré supercell have been given in Refs. [51,57]. To describe the low-energy electronic properties of TBG/BN, H^0 can be expressed in the plane-wave-like basis, as detailed in the Appendix. The Hamiltonian element between two plane-wave-like basis functions $\langle\alpha, \mathbf{K}_\xi + \mathbf{q}|H^0|\beta, \mathbf{K}_\xi + \mathbf{q} + \mathbf{Q}\rangle$ for the ξ valley is denoted by $H^0_{\xi,\alpha\beta}(\mathbf{q}, \mathbf{q} + \mathbf{Q})$ with α and β the sublattice indices, $\mathbf{q}$ a k point in the supercell Brillouin

zone (BZ), and **Q** a reciprocal lattice vector of the supercell. All the large Hamiltonian elements for the pristine TBG and the TBG/BN with the three different θ' are listed in the Supplemental Material (SM) [68] and can be used to reproduce the calculation results. The single-particle flat bands around the Fermi level (E_F) in TBG are well separated by the effective moiré potentials induced by BN, as shown in Fig. 1(b). The C_{2z} symmetry in the pristine TBG is broken in TBG/BN. In a rigid TBG/BN, the effective Hamiltonian induced by BN lacks the C_{2z} symmetry as reflected in the in-plane inversion asymmetric terms of the moiré potentials. The structural relaxation of TBG/BN also leads to the in-plane atomic deformation without the C_{2z} symmetry. The strain fields in a relaxed structure lead to modification of the on-site energies of the tight-binding Hamiltonian and also alteration of the intralayer hopping terms due to the changes of the bond lengths. The structural relaxation also breaks strongly the approximate particle-hole symmetry of the flat-band dispersions in rigid TBG, as seen in Fig. 1(b) for both relaxed TBG and TBG/BN. It can be anticipated that the full relaxation of the trilayer heterostructure in TBG/BN may give rise to greater particle-hole asymmetry in the excitation spectrums than those in TBG. It is noted that only a staggered sublattice potential is added to TBG to model the breaking of the C_{2z} symmetry due to BN in previous studies of the collective excitations of the TBG systems [46], where all the other intralayer $H^0_{\xi,\alpha\beta}(\mathbf{q}, \mathbf{q}+\mathbf{Q})$ elements with nonzero **Q** were neglected. In the full H^0, the strength of the effective moiré potential by BN varies with θ', giving rising to θ'-dependent flat bands, as shown in Fig. S1(a) of the SM. The widths of the flat bands are much larger at $\theta' = 0.54^\circ$ and -0.56° than those at 1.64°, while the valence and conduction bands are more separated at $\theta' = -0.56^\circ$. The system at $\theta' = -0.56^\circ$ also has a much smaller energy difference between the flat and remote bands due to the wider flat bands and the larger gap at E_F.

Upon inclusion of the e-e interaction, TBG/BN and TBG become Chern insulators at odd ν. We employ the self-consistent HF (SCHF) method [41,51] to obtain the mean-field ground states of the systems at odd ν; then the time dependent HF (TDHF) approach [46,66] is adopted to explore the collective excitations of TBG/BN and TBG based on the SCHF ground states as detailed in the Appendix. We first perform the HF calculations in the active-band approximation and the computationally expensive full HF calculations are then done for further exploration of the collective excitations as presented in the next section. For the active-space approximation, only the two central HF bands of each flavor are updated during the SCHF iterations and they are only expanded in the basis of the single-particle flat bands; the lower remote bands are kept frozen but still contribute to the mean-field Hartree and Fock operators of the active-band Hamiltonian. In addition, the HF operators contributed by the isolated fixed and rotated graphene layers with E_F at CNP are subtracted from the HF Hamiltonian to avoid double counting of the e-e interaction.

The HF band structures of the Chern-insulator ground states at odd ν are exhibited in Fig. 1(c) for TBG/BN with $\theta' = 0.54^\circ$ and the pristine TBG. In TBG, sublattice polarization within one layer spontaneously occurs at odd ν. In the $\xi = +$ valley, the lower band has a Chern number of $+1$ and the higher band has a Chern number of -1. The Chern numbers of the bands in the $\xi = -$ valley are just opposite to those in the $\xi = +$ valley. At each odd ν, the ground states of TBG and TBG/BN are Chern insulators with the total Chern numbers of ± 1. For each ν, three of the four flavors have the same quantitative band properties, such as the intraflavor band gaps and the bandwidths, and one flavor has different properties, which is taken to be the $(+, \uparrow)$ valley-spin flavor, as shown in Fig. 1(c). At $\nu = -1$ for TBG/BN with $\theta' = 0.54^\circ$, we have also calculated the band structures and energies of the HF states with two of the three filled bands in the same flavor and also with the total Chern numbers of ± 1. We find that such states are all metallic with overlapping HF bands and their energies are higher than the ground state with the three filled bands in three different flavors by about 20 meV per moiré supercell. It is also confirmed that the HF ground state at $\nu = 1$ has three empty bands in three different flavors. Such HF ground states at odd ν are consistent with the previous HF studies of the pristine TBG [41] and TBG/BN [51]. At a flavor with the two bands both filled or empty, the two bands of TBG/BN are well separated, while those of the pristine TBG have close energies around the $\bar{K}$ point. For TBG/BN at $\nu = -3$, the two empty bands in the same flavor are separated by 17 meV. When one flat band is filled and the other one is empty in a flavor, the intraflavor band gap (Δ_{intra}) between them in TBG/BN is much larger than that in the pristine TBG. Compared to Δ_{intra}, the interfavor band gap (Δ_{inter}) between the highest valence band in one flavor and the lowest conduction band in another flavor generally has a smaller value, so the global band gap is just Δ_{inter}. The calculated Δ_{inter} is still larger than about 10 meV at all odd ν for both the pristine TBG and TBG/BN with $\theta' = 0.54^\circ$. Such large Δ_{inter} can be due to the general trend of overestimation of the band gaps within the HF method and may be corrected by a higher theoretical level employing the density matrix renormalization group [69,70].

The HF bands at $\nu = 3$ and $\nu = 1$ appear to be the particle-hole symmetric correspondences of the bands at $\nu = -3$ and $\nu = -1$, respectively, while the band gaps can still be quite different between positive and negative ν, as shown in Figs. 1(c) and 2(b). The θ' of TBG/BN influences the quantitative properties of the HF bands, as seen in Fig. S1(b). At $\nu = \pm 3$, Δ_{inter} at $\theta' = 0.54^\circ$ is much larger than those at other θ'. The Δ_{intra} at $\theta' = -0.56^\circ$ is the largest for $\nu = 3$. In addition, when two bands in a flavor are both filled or empty, they have a much larger energy difference at $\theta' = -0.56^\circ$.

We employ the TDHF method to obtain the collective excitation modes based on the HF ground states at odd ν. We consider the collective modes with the momentum **q** expressed as [46,66]

$$|\Psi_{\{I\}}(\mathbf{q})\rangle = \sum_{I,\mathbf{k}} u_{I,\mathbf{k}}(\mathbf{q}) f^\dagger_{p_I,\mathbf{k}+\mathbf{q}} f_{h_I,\mathbf{k}} |0\rangle, \tag{1}$$

where $|0\rangle$ is the HF ground state, I represents an excitation process from the occupied band with index h_I to the empty band with the index p_I, and the operator f annihilates an electron in the HF band states. A collective mode is characterized by its set of excitation processes, which are labeled in Fig. 1(c) for the interflavor spin-wave, valley-wave, and intraflavor exciton modes. For a spin-wave mode, the h_I and p_I

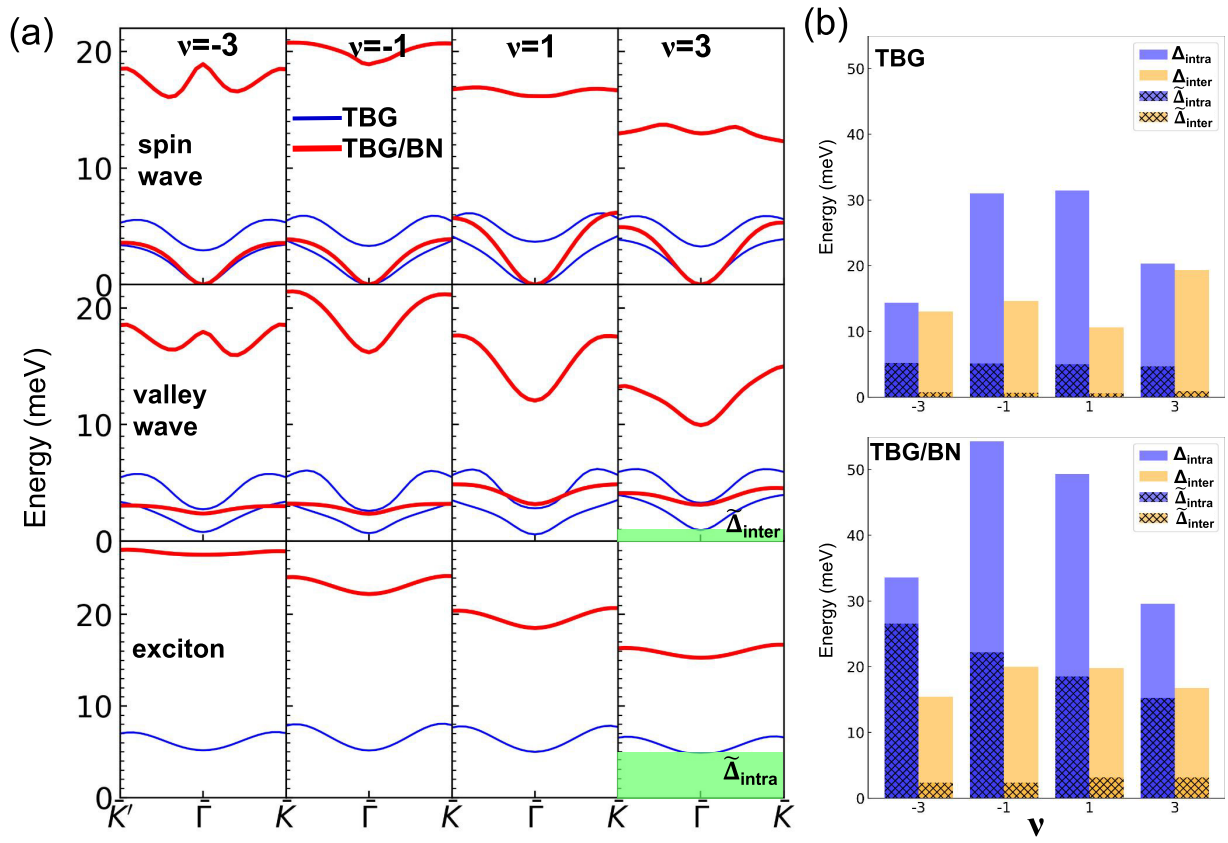

FIG. 2. Collective excitation modes of TBG/BN and the pristine TBG at odd ν. (a) The energy spectrums of the two or one lowest excitation modes as a function of the wave vector $\mathbf{q}$ for the spin-wave, valley-wave, and exciton excitations. The blue and red lines represent the excitation bands of the pristine TBG and the TBG/BN at $\theta' = 0.54^\circ$, respectively. $\bar{K}'$ in the k-point path is just the opposite of $\bar{K}$. The valley-wave excitation gap ($\tilde{\Delta}_{\text{inter}}$) and the exciton excitation gap ($\tilde{\Delta}_{\text{intra}}$) at $\mathbf{q} = \mathbf{0}$ are labeled by the green shades. The tilde in $\tilde{\Delta}$ is used to differentiate the excitation gap from the HF band gap Δ. (b) The HF band gaps and the corresponding excitation gaps at different ν for TBG/BN and TBG.

states have the same valley but the opposite spin indexes and their valley-spin indexes are respectively taken to be $(+\uparrow)$ and $(+\downarrow)$ at $\nu = -3$ as an example. For a valley-wave mode, the h_I and p_I states have the same spin index but the opposite valley index and their valley-spin indexes are respectively taken to be $(+\uparrow)$ and $(-\uparrow)$ at $\nu = -3$ as an example. The h_I and p_I states for an exciton mode have both the same valley and spin indexes and are taken to be in the flavor with one filled flat band and one empty flat band.

For the pristine TBG, all the excitation spectrums exhibit approximate particle-hole symmetry and are almost the same for all odd ν, as shown in Fig. 2(a). The spin-wave mode has a zero excitation gap, the valley-wave mode has an extremely small gap of about 0.5 meV, and the exciton mode has a gap of about 5 meV. Such finite gaps of the valley-wave and exciton modes are slightly larger than those predicted for the TBG described by the Bistritzer-MacDonald model [66], which can be attributed to the in-plane structural deformation in the relaxed TBG. For the pristine TBG, both the spin-wave and valley-wave excitations have two low-energy collective modes in the gap at each $\mathbf{q}$. In contrast, the excitation spectrum of TBG/BN at positive ν is rather different from those at negative ν and those with the same sign of ν are quite similar. The lowest spin-wave mode at positive ν has a larger spectrum width than that at negative ν but they all have zero excitation gap. For the valley wave, all the excitation energies are higher than 2.5 meV, which is much larger than that of the pristine TBG. This is consistent with Ref. [46] for TBG with a sublattice potential difference. The valley wave has a higher excitation gap ($\tilde{\Delta}_{\text{inter}}$) at positive ν. For both the spin wave and the valley wave, the lowest modes become much more apart than those in TBG. The lowest exciton modes of TBG/BN have much higher energies than those of TBG. The exciton gap ($\tilde{\Delta}_{\text{intra}}$) decreases with ν from -3 to 3, with the gap still reaching about 16 meV at $\nu = 3$.

In comparison to the HF band gaps, the $\tilde{\Delta}_{\text{inter}}$ of the valley wave modes are much smaller than the Δ_{inter} for both TBG and TBG/BN, while the $\tilde{\Delta}_{\text{intra}}$ of the exciton modes of TBG/BN reaches about half of the Δ_{intra}, which is a significant contrast to the much smaller $\tilde{\Delta}_{\text{intra}}/\Delta_{\text{intra}}$ for TBG, as shown in Fig. 2(b). For the exciton modes, the two-body exciton wave function as a function of the electron ($\mathbf{r}_e$) and hole ($\mathbf{r}_h$) positions can be calculated as

$$\Psi(\mathbf{r}_e, \mathbf{r}_h) = \frac{1}{N_{\mathbf{k}}} \sum_{\mathbf{k}} u_{\mathbf{k}} \psi_{p\mathbf{k}}(\mathbf{r}_e) \psi^*_{h\mathbf{k}}(\mathbf{r}_h), \tag{2}$$

where $\psi_{p\mathbf{k}}$ and $\psi_{h\mathbf{k}}$ are the HF conduction and valence band states corresponding to the exciton excitation. Figure 3 exhibits the wave function of the lowest exciton mode at $\mathbf{q} = \mathbf{0}$

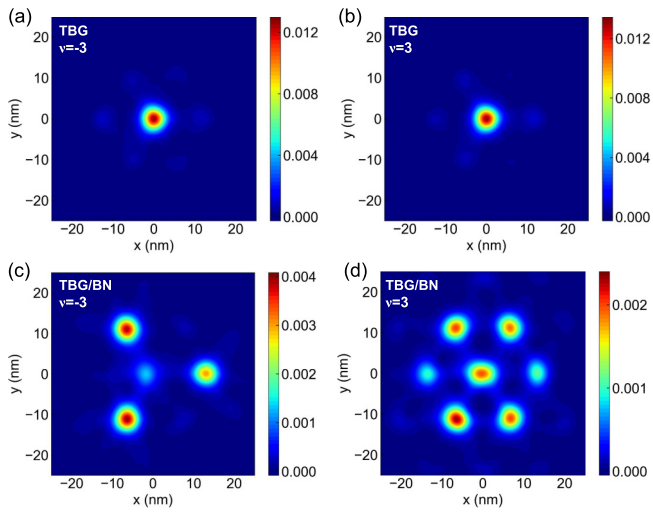

FIG. 3. Spatial distribution ($|\Psi(\mathbf{r}_e, \mathbf{r}_h)|^2$) of the exciton wave function of the lowest mode at $\mathbf{q} = \mathbf{0}$ as a function of the electron position $\mathbf{r}_e$ with the hole position $\mathbf{r}_h$ at the origin of a supercell where the bilayer is locally AA stacked for TBG at $\nu = -3$ (a), $\nu = 3$ (b), and TBG/BN with $\theta' = 0.54^\circ$ at $\nu = -3$ (c), $\nu = 3$ (d).

with $\mathbf{r}_h$ at the origin of a supercell where the bilayer graphene is locally AA stacked. The particle and hole are strongly bound at all the odd ν for the pristine TBG with the particle localized around the origin. The spatial map of the exciton wave functions in TBG/BN spread a much larger range with the particle mainly distributed around the nonzero smallest superlattice vectors. Unlike TBG, TBG/BN at $\nu = 3$ has a quite different exciton wave function from that at $\nu = -3$ with the wave function at $\nu = 3$ less spatially localized.

The quantitative behavior of the excitation spectrum varies with θ', as seen in Fig. 4. The systems with the negative θ' of -0.56° tend to have a smaller valley-wave excitation energy, while their exciton energies are much higher than those at positive θ' for the positive ν. For the valley-wave modes, the $\tilde{\Delta}_{\text{inter}}$ at the two positive θ' have similar values for the negative ν, while they differ by about 1 meV for the positive ν. The exciton energy at $\theta' = 0.54^\circ$ is higher than that at $\theta' = 1.64^\circ$ for the negative ν but has similar values for the positive ν. The excitation spectrums of TBG/BN with $\theta' = 0.54^\circ$ at $\nu = \pm 3$ are also compared with those of the system with only the staggered sublattice potential difference in H^0 of 16 meV and with all the other intralayer $H^0_{\xi,\alpha\beta}(\mathbf{q}, \mathbf{q} + \mathbf{Q})$ elements with nonzero $\mathbf{Q}$ neglected in Fig. 4(b). Their rather different single-particle and HF band structures are displayed in Fig. S2 of the SM. The excitation spectrums of TBG with the staggered potential are approximately particle-hole symmetric at $\nu = \pm 3$, which is similar to the pristine TBG but contrasts with TBG/BN. For the spin-wave and valley-wave modes, the lowest excitation energy bands of the two systems have similar values, while the second bands of TBG/BN are much higher. For the exciton modes, the lowest excitation energies of TBG/BN are much larger than those of TBG with only the staggered potential. In experiments, particle-hole asymmetry has been observed for the low-energy response properties of the correlated states

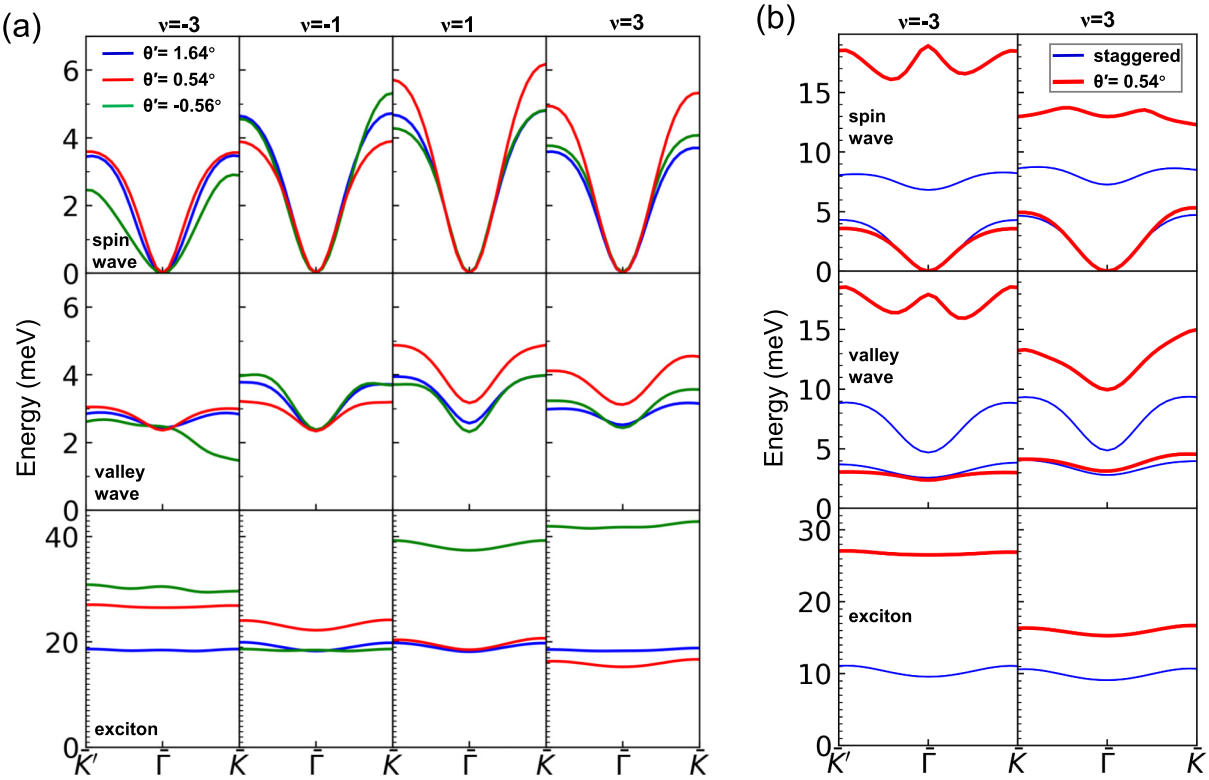

FIG. 4. (a) Energy spectrums of the lowest spin-wave, valley-wave, and exciton excitation modes at different ν for TBG/BN with $\theta' = 1.64^\circ$, 0.54°, and -0.56°. (b) The excitation spectrums for TBG with only the staggered sublattice potential difference in H^0 of 16 meV (blue lines) and TBG/BN with $\theta' = 0.54^\circ$.

in TBG [11,17–19,62,64]. The comparative calculations of the collective excitation modes in the pristine TBG, the TBG with staggered potential, and TBG/BN thus suggest that the full Hamiltonian of TBG, especially the nonlocal effect and the relaxation effect with TBG under various external perturbations such as alignment with BN, is required to understand the experimentally observed particle-hole asymmetry in TBG. Regarding the possible experimental verification of our computational predictions, the behavior of the spin-wave and valley-wave modes in TBG/BN at different excitation energies can be compared for the positive and negative ν in experiments to show whether the observations of the excitations at positive and negative ν are more different at a higher energy. Moreover, the rather distinct exciton energies of TBG/BN at $\nu = \pm 3$ may be confirmed in the future experimental measurements of the interband optical transitions of the Chern insulators in TBG/BN.

III. FULL HF BANDS AND EXCITATIONS

Since the remote bands are frozen in the active-band approximation of the SCHF calculations, the excitation processes between the remote and flat bands have been ignored and the quantitative properties of the flat bands can be modified when the remote bands are allowed to be updated in the SCHF calculations. Full SCHF calculations have also been performed to obtain the full HF bands of TBG/BN and the excitation spectrums are computed by considering the excitation processes between the five highest valence HF bands and the five lowest conduction HF bands. It is noted that the convergent spin-wave spectrum requires the possible excitation processes between all the HF bands, which are beyond our calculation capability, so only the interflavor valley-wave and the intraflavor exciton modes are considered based on the full SCHF ground states.

To compare the active-band approximation with the full SCHF description of the central HF bands, the projection of each HF band state on the single-particle flat bands is computed as $\sum_m |\langle\psi^0_m(\sigma,\mathbf{k})|\psi_i(\sigma,\mathbf{k})\rangle|^2$ with $|\psi^0_m(\sigma,\mathbf{k})\rangle$ representing the two single-particle flat-band states of flavor σ and $|\psi_i\rangle$ a HF band state. We find that at a k point rather away from the $\bar{\Gamma}$ point, only two low-energy HF band states of a flavor are mainly contributed by the single-particle flat-band states, as shown in Fig. 5 for TBG/BN with $\theta' = 0.54°$. These HF bands are termed as flatlike bands to distinguish them from the single-particle flat bands. In contrast, several other HF bands near the $\bar{\Gamma}$ point can have substantial contribution from the flat-band states, especially for the flavor with one flatlike band occupied and the other flatlike band empty. In particular, the flat-band contribution becomes very small for some low-energy HF states at $\bar{\Gamma}$. When the flatlike bands of a flavor are both occupied or empty, they are generally well separated from the remote bands and the intraflavor gap around E_F between the remote and flatlike bands is denoted by Δ'_{intra}. The flatlike bands become entangled with the remote bands when E_F lies between them and the intraflavor gap between these flatlike bands is denoted by Δ_{intra}. Similar to the active-band approximation, the interflavor gap Δ_{inter} is also between the flatlike bands. For the full HF bands, the global gap among all flavors is just Δ'_{intra}. Δ_{intra} has large and similar values

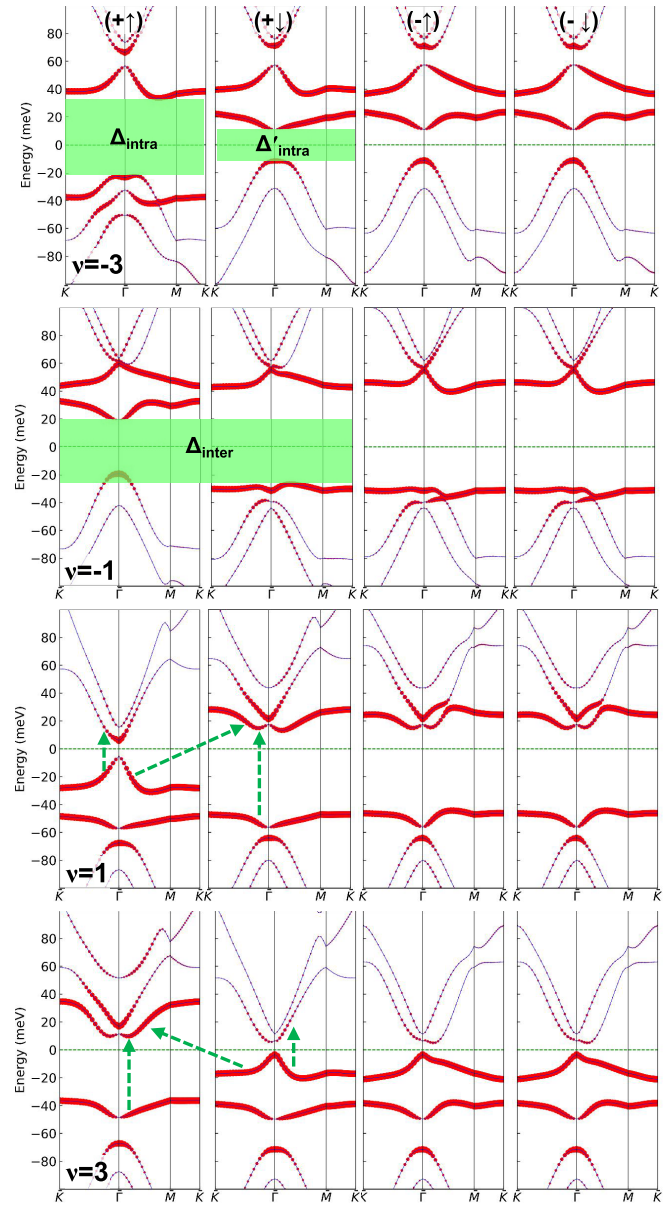

FIG. 5. Full HF band structures of TBG/BN at $\theta' = 0.54°$ for each flavor at different ν. The magnitude of the projection of each HF band state on the single-particle flat bands is represented by the size of the red circle. The band gap Δ_{intra} between the intraflavor flatlike bands, the Δ_{inter} between the interflavor flatlike bands, and the Δ'_{intra} between the remote and flatlike bands are labeled by the green shades. The interflavor valley-wave excitation mainly between the flatlike bands, the intraflavor exciton excitation mainly between the flatlike bands, and the intraflavor exciton excitation mainly between the flatlike bands and the remote bands are indicated by the dashed green lines.

for all the negative and positive ν, which is similar to the active-band approximation. However, the systems at positive ν have much smaller Δ'_{intra} and Δ_{inter} than those at negative ν, which indicates the strong breaking of the particle-hole symmetry for the full HF band structures. At each ν, there are also three flavors with the same quantitative band properties, as seen in Fig. 5.

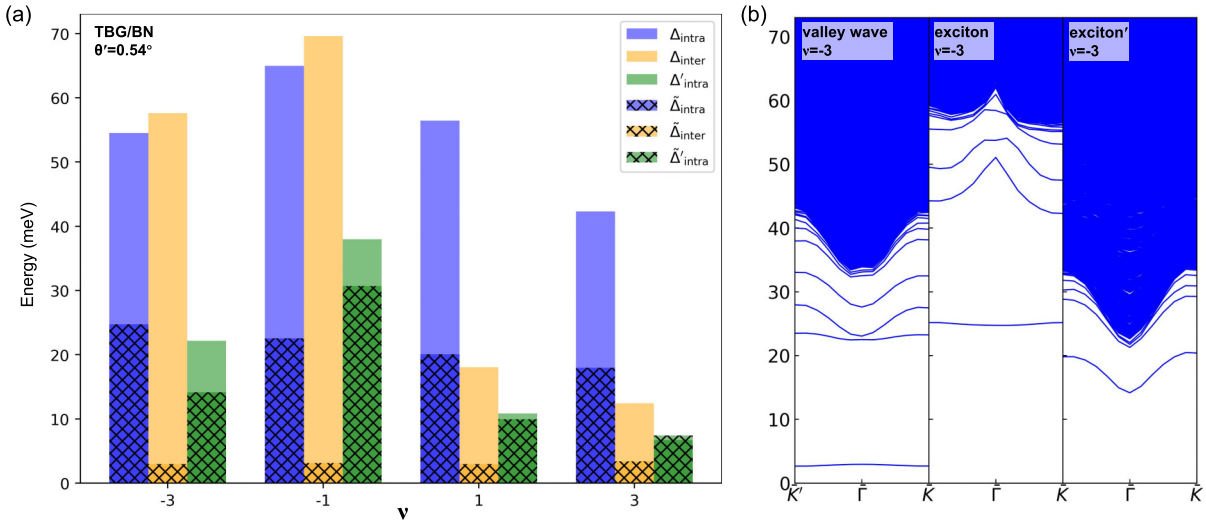

FIG. 6. (a) Band gaps Δ_{intra}, Δ_{inter}, and Δ'_{intra} and the corresponding excitation gaps $\tilde{\Delta}_{\text{intra}}$, $\tilde{\Delta}_{\text{inter}}$, and $\tilde{\Delta}'_{\text{intra}}$ from the full HF calculations at different ν for TBG/BN with $\theta' = 0.54°$. (b) The energy spectrums for the valley-wave excitation, the exciton excitation mainly between flatlike bands, and the exciton excitation (dented by exciton′) mainly between empty flatlike bands and the filled remote bands at $\nu = -3$.

We consider the interflavor valley-wave excitation modes corresponding to Δ_{inter} and the intraflavor exciton modes corresponding to Δ_{intra} and Δ'_{intra}, based on the full HF ground states. The excitation spectrum and the excitation gaps of these modes are displayed in Fig. 6 for TBG/BN with $\theta' = 0.54°$. The valley-wave excitation gap $\tilde{\Delta}_{\text{inter}}$ becomes slightly higher than that obtained from the active-band approximation and reaches about 3 meV, but is still rather small compared with Δ_{inter}. The excitation gaps $\tilde{\Delta}_{\text{intra}}$ of the exciton modes between the flatlike bands have similar values as those from the active-band approximation and are below half of Δ_{intra}. In contrast, the gaps ($\tilde{\Delta}'_{\text{intra}}$) of the exciton modes between the flatlike bands and the remote bands are just slightly smaller than Δ'_{intra}. This indicates that the exciton modes between the flatlike bands and the remote bands are composed of weak-bound particle-hole pairs, while strong binding of the particle-hole pairs occurs in the exciton modes between the flatlike bands. At $\nu = -3, 1, 3$, $\tilde{\Delta}_{\text{intra}}$ is higher than $\tilde{\Delta}'_{\text{intra}}$ and even the gap Δ'_{intra}. Only at $\nu = 1$ does $\tilde{\Delta}_{\text{intra}}$ have a lower value than $\tilde{\Delta}'_{\text{intra}}$. In addition, the excitation energies of the lowest modes for the exciton modes between the flatlike bands and the remote bands are much more dispersive as a function of $\mathbf{q}$ than those of the valley-wave modes and the exciton modes between the flatlike bands, as shown in Fig. 6(b).

The optical properties of the Chern insulators are determined by the intraflavor exciton modes and the optical conductivity within the TDHF method is given by [66]

$$\text{Re}\sigma_{xx} = \frac{\gamma}{\hbar\omega N_{\mathbf{k}}\Omega_0}\sum_i \frac{1}{(\hbar\omega - \hbar\omega_i)^2 + \gamma^2} \times \sum_{I\mathbf{k},I'\mathbf{k}'} J^*_{x,I\mathbf{k}} u_{i,I\mathbf{k}} u^*_{i,I'\mathbf{k}'} J_{x,I'\mathbf{k}'}, \quad (3)$$

where ω is the frequency of the incident light, $\hbar\omega_i$ is the energy of an exciton mode labeled by i, u_i is the state vector of the exciton mode, $J_{x,I\mathbf{k}} = \langle\psi_{pI\mathbf{k}}| - e/\hbar\partial H_k/\partial k_x|\psi_{hI\mathbf{k}}\rangle$ is the element of the current density operator between the empty and occupied states of the excitation process I, γ is a small energy for broadening of the excitation energy, Ω_0 is the area of the moire supercell, and $N_{\mathbf{k}}$ is the number of k points. So at $\omega = \omega_i$, the contribution of the exciton mode i to σ_{xx} is proportional to $\sigma_i \equiv \hbar^2/(e^2 N_{\mathbf{k}}) \sum_{I\mathbf{k},I'\mathbf{k}'} J^*_{x,I\mathbf{k}} u_{i,I\mathbf{k}} u^*_{i,I'\mathbf{k}'} J_{x,I'\mathbf{k}'}$. We find that the σ_i of the lowest exciton mode between the remote and flatlike bands at $\nu = -3$ reaches 0.102 eV Å^2 and is even much larger than that of the lowest exciton mode between the flatlike bands, which is just 0.022 eV Å^2. Therefore, the lowest-frequency optical properties associated with the intraflavor excitations are mainly determined by the exciton modes between the remote bands and the flatlike bands at $\nu = -3, 1, 3$, while they are mainly contributed by the exciton mode between the flatlike bands at $\nu = -1$.

At the other two θ' of 1.64° and −0.56°, Δ'_{intra} from the full SCHF calculations can become larger than Δ_{inter}, but are all much smaller than Δ_{intra}, as seen in Figs. S3 and S4 of the SM [68]. For $\theta' = -0.56°$, the system at $\nu = -3$ becomes metallic with the highest occupied band of the $(+,\uparrow)$ flavor slightly overlapping with the lowest empty bands of other flavors. The systems at $\theta' = 1.64°$ generally have smaller Δ'_{intra} than those at other θ'. For the exciton modes, the excitation gaps $\tilde{\Delta}'_{\text{intra}}$ are also much smaller than $\tilde{\Delta}_{\text{intra}}$ and the systems with $\theta' = -0.56°$ have the largest $\tilde{\Delta}_{\text{intra}}$, as seen in Fig. S4 of the SM. In addition, $\tilde{\Delta}'_{\text{intra}}$ can even become larger than the indirect gap Δ'_{intra} for some systems with θ' of 1.64° and −0.56°. The $\tilde{\Delta}_{\text{inter}}$ for the valley-wave modes all have similar values of about 3 meV.

IV. SUMMARY AND CONCLUSIONS

In the 1×1 commensurate supercells of TBG/BN, the single-particle flat bands around E_F are gapped due to the broken C_{2z} symmetry and the SCHF ground states at odd ν are the Chern insulators with flavor-polarized HF bands. In the active-band approximation, the two active HF bands in the same flavor are well separated in TBG/BN when they are

both filled or empty and the intraflavor gap Δ_{intra} in TBG/BN is much larger than that in the pristine TBG. The energy spectrums of the collective excitation modes for the Chern insulator states are obtained with the TDHF method. The spin-wave modes in both TBG/BN and TBG have a zero excitation gap, while the gaps of the valley-wave and exciton modes in TBG/BN are much larger than those in TBG. The excitation gaps $\tilde{\Delta}_{\text{inter}}$ and $\tilde{\Delta}_{\text{intra}}$ in TBG/BN reach about 2.5 meV and 20 meV, respectively, with $\tilde{\Delta}_{\text{intra}}$ almost half of the intraflavor band gap Δ_{intra}. In contrast to TBG with almost particle-hole symmetric excitation modes for positive and negative ν, the excitation spectrums and gaps of TBG/BN at positive ν are rather different from those at negative ν. The exciton wave functions in TBG are also much more spatially localized than those in TBG/BN. Full SCHF calculations show that more HF bands besides the two central bands can have rather large contribution from the single-particle flat-band states in TBG/BN and the intraflavor gap Δ_{intra} between the flatlike bands is much larger than the Δ'_{intra} between the remote and flatlike bands. The excitation gap $\tilde{\Delta}'_{\text{intra}}$ of the exciton modes between the remote and flatlike bands is just slightly smaller than Δ'_{intra}, but is generally lower than the $\tilde{\Delta}_{\text{intra}}$ between the flatlike bands, so the optical properties of the Chern insulator states are mainly determined by the exciton modes between the remote and flatlike bands. The valley-wave modes from full HF calculations have similar energies as those in the active-band approximation. In addition, the quantitative behavior of the excitation spectrums varies with θ' of TBG/BN.

ACKNOWLEDGMENTS

We gratefully acknowledge valuable discussions with D. Tománek, Y. Yin, and X. Xiong. This research was supported by the National Natural Science Foundation of China (Grants No. 11974312 and No. 92270104) and the Open Research Fund of CNMGE Platform & NSCC-TJ.

APPENDIX

1. Geometry of the moiré superlattice

In the trilayer heterostructures of TBG/BN, moiré superlattices arise between the graphene layers and between the middle graphene layer and BN, as shown in Fig. 1(a). To establish the geometry of TBG/BN, the middle graphene layer (G1) is taken to be fixed, the top graphene layer (G2) is rotated by θ counterclockwise, the bottom BN layer is rotated by θ' counterclockwise (positive θ') or clockwise (negative θ'), and graphene has a smaller lattice constant (a_G) than that (a_{BN}) of BN by $\epsilon = a_G/a_{BN} - 1$. The *ab initio* calculations using the local density approximation (LDA) [71] functional give $a_G = 2.447$ Å and $\epsilon = -1.70\%$. A position $\mathbf{r}$ in G1 is transformed to $T_\theta \mathbf{r}$ in G2 and $S\mathbf{r}$ in BN with T_θ the rotation matrix by θ and $S = T_{\theta'}/(1+\epsilon)$. When G2 and BN have not been rotated, the spanning vectors of a unit cell of the honeycomb lattice in each layer are taken to be $\mathbf{a_1} = a[\sqrt{3}/2, -1/2]$ and $\mathbf{a_2} = a[\sqrt{3}/2, 1/2]$, where a is the lattice constant of graphene or BN. The sublattice-A and sublattice-B atoms in a graphene or BN unit cell are located at $(\mathbf{a_1}+\mathbf{a_2})/3$ and $(2\mathbf{a_1}+2\mathbf{a_2})/3$, respectively. At $\theta = 1.0845^\circ$ around the magic-angle of TBG, the moiré superlattice in G2/G1 becomes exactly periodic with the supercell spanned by the basis vectors $\mathbf{L_1} = N\mathbf{a_1} + (N+1)\mathbf{a_2}$ and $\mathbf{L_2} = T_{60^\circ}\tilde{\mathbf{L}}_\mathbf{1} = -(N+1)\mathbf{a_1} + (2N+1)\mathbf{a_2}$ at $N = 30$. Such a 1×1 supercell becomes commensurate with the moiré superlattices in G2/BN when $(S^{-1} - I)\tilde{\mathbf{L}}_\mathbf{1} = -\mathbf{a_2} + m(\mathbf{a_1} - \mathbf{a_2})$ at $\theta' = 1.64^\circ, 0.54^\circ, -0.56^\circ$ with $m = 1, 0, -1$, respectively [51,56–59]. The reciprocal lattice of the 1×1 commensurate supercell of TBG/BN is spanned by $\mathbf{b}_\mathbf{1}^{(\mathbf{s})} = 2\pi/(1 + 3N + 3N^2)/a[(2+3N)/\sqrt{3}, -N]$ and $\mathbf{b}_\mathbf{2}^{(\mathbf{s})} = 2\pi/(1 + 3N + 3N^2)/a[-1/\sqrt{3}, 1+2N]$.

2. Single-particle Hamiltonian

We employ the effective single-particle tight-binding Hamiltonian ($\hat{H}^0$) of a relaxed TBG/BN commensurate supercell in Refs. [51,57] to obtain its single-particle Hamiltonian elements in the plane-wave-like basis. The tight-binding model of $\hat{H}^0$ reads

$$\hat{H} = \sum_{n=1}^{2}\sum_{i}\varepsilon_{n,i}c_{n,i}^{\dagger}c_{n,i} + \sum_{n=1}^{2}\sum_{\langle i,j\rangle}t_{\langle i,j\rangle}^{(n,n)}(c_{n,i}^{\dagger}c_{n,j} + \text{H.c.}) + \sum_{i,j}t_{i,j}^{(1,2)}(c_{1,i}^{\dagger}c_{2,j} + \text{H.c.}), \tag{A1}$$

where $c_{n,i}^{\dagger}$ ($n = 1, 2$) is the creation and $c_{n,i}$ is the annihilation operator of a p_z-like orbital at the site i in the Gn layer and $\langle i, j\rangle$ denotes the intralayer nearest neighbors. The dependence of intralayer on-site energies ($\varepsilon_{n,i}$) and hopping terms ($t_{\langle i,j\rangle}^{(n,n)}$) and the interlayer hopping terms ($t_{i,j}^{(1,2)}$) on the site positions in relaxed TBG/BN were given in Refs. [51,57]. In the plane-wave-like basis, the basis functions are labeled with the valley index ($\xi = \pm$), the sublattice and layer index ($\alpha =$ A1, B1, A2, B2), a k point ($\mathbf{k}$) in the supercell BZ, and a reciprocal lattice vector ($\mathbf{G}$) of the supercell. They are defined as [51,57]

$$|\alpha, \mathbf{k} + \mathbf{K}_\xi + \mathbf{G}\rangle = \frac{1}{\sqrt{\tilde{N}}}\sum_{\mathbf{r}_\alpha} e^{i(\mathbf{k}+\mathbf{K}_\xi+\mathbf{G})\cdot\mathbf{r}_\alpha}|\mathbf{r}_\alpha\rangle, \tag{A2}$$

where $\mathbf{K}_\xi$ is the center of one of the supercell BZs containing the Dirac points of G1 at their corners in the ξ valley and $\mathbf{r}_\alpha$ is the rigid in-plane position of a site in the sublattice α of the corresponding layer. $\mathbf{K}_+$ is taken to be $-N\mathbf{b}_\mathbf{2}^{(\mathbf{s})}$ and $\mathbf{K}_- = -\mathbf{K}_+$. The H^0 element between two basis functions is given by [51,57]

$$\langle\alpha, \mathbf{K}_\xi + \mathbf{q}|\hat{H}^0|\beta, \mathbf{K}_\xi + \mathbf{q} + \mathbf{Q}\rangle = \frac{1}{N}\sum_{\mathbf{r}_\alpha\in SC}\sum_{\mathbf{r}_\beta} e^{-i(\mathbf{K}_\xi+\mathbf{q})\cdot\mathbf{r}_\alpha + i(\mathbf{K}_\xi+\mathbf{q}+\mathbf{Q})\cdot\mathbf{r}_\beta}\langle\mathbf{r}_\alpha|\hat{H}^0|\mathbf{r}_\beta\rangle, \tag{A3}$$

where $\mathbf{q}$ is a k point in the supercell reciprocal space and $\mathbf{Q}$ is a supercell reciprocal lattice vector. The summation over $\mathbf{r}_\alpha$ is done in a supercell and N is the number of graphene unit cells in one layer of the supercell. $\langle\mathbf{r}_\alpha|\hat{H}^0|\mathbf{r}_\beta\rangle$ represents the on-site and hopping terms in the tight-binding Hamiltonian.

The H^0 elements with norm larger than 0.2 meV are included for the calculations. The large H^0 elements are listed in Tables SI– SV of the SM [68] to compare the different H^0 of the pristine TBG and TBG/BN with varying θ' and can be used to reproduce our results. The Hamiltonian element

$\langle \alpha, \mathbf{K}_\xi + \mathbf{q}|H^0|\beta, \mathbf{K}_\xi + \mathbf{q} + \mathbf{Q}\rangle$ for the ξ valley is denoted by $H^0_{\xi,\alpha\beta}(\mathbf{q}, \mathbf{q}+\mathbf{Q})$. The nonlocality of $\hat{H}^0$ is fully taken into account with $H^0_{\xi,\alpha\beta}(\mathbf{q}, \mathbf{q}+\mathbf{Q})$ depending both on $\mathbf{q}$ and $\mathbf{Q}$ and the expansion of each element up to linear order of $\mathbf{q}$ as $C_0 + C_x q_x + C_y q_y$ is given in the SM. The time reversal symmetry in H^0 leads to $H^0_{-,\alpha\beta}(\mathbf{q}, \mathbf{q}+\mathbf{Q}) = H^{0*}_{+,\alpha\beta}(-\mathbf{q}, -\mathbf{q}-\mathbf{Q})$ and the Hermiticity of the H^0 matrix gives $H^0_{\xi,\beta\alpha}(\mathbf{q}, \mathbf{q}+\mathbf{Q}) = H^{0*}_{\xi,\alpha\beta}[\mathbf{q}+\mathbf{Q}, (\mathbf{q}+\mathbf{Q}) - \mathbf{Q}]$. So only the H^0 elements with $\alpha \leqslant \beta$ and $\xi = +$ are listed.

The listed H^0 elements show that the interlayer Hamiltonian is almost unaffected by alignment with BN. For the intralayer Hamiltonian in G2, the elements $H^0_{+,\alpha\beta}(\mathbf{q}, \mathbf{q}+\mathbf{Q})$ with $\alpha =$ A2, $\beta =$ B2, and $|\mathbf{Q}| = |\mathbf{b}^{(s)}_1|$ have almost the same amplitude for all systems and their nonzero values are due to the relaxation induced modulation of the intralayer hopping. However, three of the six $H^0_{+,\alpha\beta}(\mathbf{q}, \mathbf{q}+\mathbf{Q})$ elements with $\alpha =$ A1, $\beta =$ B1, and $|\mathbf{Q}| = |\mathbf{b}^{(s)}_1|$ of TBG/BN are much larger than those of the pristine TBG, indicating that the spatial modulation of the intralayer hopping becomes stronger upon alignment with BN and the C_{2z} symmetry is broken. The $\mathbf{Q}$ with the large elements depends on θ' of TBG/BN and the phases of the complex values of the elements vary with θ'. Both the intralayer and interlayer Hamiltonian exhibit nonlocality. The alignment with BN greatly enhances the nonlocality of the intralayer Hamiltonian in G1, while it does not affect that of the interlayer Hamiltonian.

3. Self-consistent HF and time-dependent HF methods

For a valley-spin flavor, each plane-wave basis state with momentum $\mathbf{k}$ in the sublattice α corresponds to a creation operator $c^\dagger_{\mathbf{k},\alpha\mu}$, where μ indexes the flavor. Then the e-e interaction Hamiltonian can be expressed as

$$\hat{H}_{ee} = \frac{1}{2N}\sum V(\mathbf{q}) c^\dagger_{\mathbf{k}+\mathbf{q},\alpha\mu} c^\dagger_{\mathbf{k}'-\mathbf{q},\beta\mu'} c_{\mathbf{k}',\beta\mu'} c_{\mathbf{k},\alpha\mu}, \quad \text{(A4)}$$

where $V(\mathbf{q}) = e^2/(\Omega 4\pi\epsilon_r\epsilon_0)2\pi/|\mathbf{q}|$ with Ω the supercell area and the dielectric constant ϵ_r is taken to be 10 considering the screening by both the BN substrates and electric gates. We consider the correlated insulator states at odd ν with flavor-polarized HF band states.

In the mean-field HF Hamiltonian [41,51], the Fock operator ($\hat{\Sigma}^F$) is expressed as

$$\hat{\Sigma}^F = -\frac{1}{N_\mathbf{k}} \sum_{\mu\alpha\beta\mathbf{kq}} \sum_{\mathbf{G}'+\mathbf{Q}'=\mathbf{G}+\mathbf{Q}} V(|\mathbf{k}+\mathbf{G}-\mathbf{q}-\mathbf{Q}'|) \times \langle c^\dagger_{\mathbf{q}+\mathbf{Q}',\beta\mu} c_{\mathbf{q}+\mathbf{Q},\alpha\mu}\rangle\, c^\dagger_{\mathbf{k}+\mathbf{G}',\alpha\mu} c_{\mathbf{k}+\mathbf{G},\beta\mu}. \quad \text{(A5)}$$

The $\langle c^\dagger_{\mathbf{q}+\mathbf{Q}',\beta\mu} c_{\mathbf{q}+\mathbf{Q},\alpha\mu}\rangle$ is the density matrix element and is denoted by $\rho_{\beta\mathbf{Q}',\alpha\mathbf{Q}}(\mu, \mathbf{q})$. Then the matrix elements of $\hat{\Sigma}^F$ for each μ and $\mathbf{k}$ are

$$\Sigma^F_{\alpha\mathbf{G}',\beta\mathbf{G}}(\mu, \mathbf{k}) = -\frac{1}{N_\mathbf{k}} \sum_{\mathbf{q}} \sum_{\mathbf{G}'+\mathbf{Q}'=\mathbf{G}+\mathbf{Q}} V(|\mathbf{k}+\mathbf{G} - \mathbf{q} - \mathbf{Q}'|)\, \rho_{\beta\mathbf{Q}',\alpha\mathbf{Q}}(\mu, \mathbf{q}). \quad \text{(A6)}$$

ρ is calculated from the HF band states as

$$\rho_{\beta\mathbf{Q}',\alpha\mathbf{Q}}(\mu, \mathbf{q}) = \sum_{n=occ} \psi^*_{n,\beta\mathbf{Q}'}(\mu, \mathbf{q})\psi_{n,\alpha\mathbf{Q}}(\mu, \mathbf{q}), \quad \text{(A7)}$$

where $\psi_n(\mu, \mathbf{q})$ represents an occupied HF band state with the flavor μ at the k point $\mathbf{q}$ in the supercell BZ. The Fock operator ($\hat{\Sigma}^H$) is given by

$$\hat{\Sigma}^H = \frac{1}{N_\mathbf{k}} \sum_{\mu\sigma\alpha\beta\mathbf{kq}} \sum_{\mathbf{G}'+\mathbf{Q}'=\mathbf{G}+\mathbf{Q}} V(|\mathbf{Q}-\mathbf{Q}'|) \times \langle c^\dagger_{\mathbf{q}+\mathbf{Q}',\beta\sigma} c_{\mathbf{q}+\mathbf{Q},\beta\sigma}\rangle\, c^\dagger_{\mathbf{k}+\mathbf{G}',\alpha\mu} c_{\mathbf{k}+\mathbf{G},\alpha\mu}. \quad \text{(A8)}$$

The matrix elements of $\hat{\Sigma}^H$ do not depend on μ and $\mathbf{k}$ and can be expressed as

$$\Sigma^H_{\alpha\mathbf{G}',\alpha\mathbf{G}} = \frac{1}{N_\mathbf{k}} \sum_{\sigma\beta\mathbf{q}} \sum_{\mathbf{G}'+\mathbf{Q}'=\mathbf{G}+\mathbf{Q}} V(|\mathbf{Q}-\mathbf{Q}'|)\, \rho_{\beta\mathbf{Q}',\beta\mathbf{Q}}(\sigma, \mathbf{q}). \quad \text{(A9)}$$

The Fock matrix (Σ^F_{iso}) contributed by the density matrix (ϱ_{iso}) of the isolated fixed and rotated graphene layers at CNP is subtracted from the HF Hamiltonian to avoid double counting of the e-e interaction. The Hartree term contributed by ϱ_{iso} is zero. Then the HF Hamiltonian matrix for the SCHF calculations becomes

$$H = H^0 + \Sigma^H + \Sigma^F - \Sigma^F_{\text{iso}}. \quad \text{(A10)}$$

For the active-band approximation, the filled remote bands are frozen and the states in the two active low-energy HF bands are only projected on the two single-particle flat-band states of each flavor. The projected HF Hamiltonian matrix of the two active bands in the basis of the single-particle flat bands for each flavor and k point can be obtained by

$$\tilde{H}_{mn} = \psi^{0\dagger}_m H \psi^0_n, \quad \text{(A11)}$$

where ψ^0_n is the single-particle flat-band state vector in the plane-wave basis. The obtained active bands from $\tilde{H}$ and the frozen bands are then used to calculate the density matrix ρ in the plane-wave basis by Eq. (A7), which gives the H in Eq. (A10).

Within the TDHF method [51,57], the excitation modes in Eq. (1) can be obtained by the eigenvalue equation

$$[A(\mathbf{q}) + \Delta(\mathbf{q})]u(\mathbf{q}) = \omega(\mathbf{q})u(\mathbf{q}), \quad \text{(A12)}$$

where $\omega(\mathbf{q})$ represents the excitation energy. $\Delta(\mathbf{q})$ is a diagonal matrix with $\Delta_{I\mathbf{k}}(\mathbf{q}) = \varepsilon_{p_I}(\mathbf{q}+\mathbf{k}) - \varepsilon_{h_I}(\mathbf{k})$, and $\varepsilon_n(\mathbf{k})$ is the HF band energy. The matrix element of $A(\mathbf{q})$ is

$$\begin{aligned} A_{I\mathbf{k},J\mathbf{k}'}(\mathbf{q}) &= \langle \psi_{p(\mathbf{k}+\mathbf{q})}(\mathbf{r})\psi_{h'\mathbf{k}'}(\mathbf{r}')|V(\mathbf{r}-\mathbf{r}')|\psi_{h\mathbf{k}}(\mathbf{r})\psi_{p'(\mathbf{k}'+\mathbf{q})}(\mathbf{r}')\rangle \\ &\quad - \langle \psi_{p(\mathbf{k}+\mathbf{q})}(\mathbf{r})\psi_{h'\mathbf{k}'}(\mathbf{r}')|V(\mathbf{r}-\mathbf{r}')|\psi_{p'(\mathbf{k}'+\mathbf{q})}(\mathbf{r})\psi_{h\mathbf{k}}(\mathbf{r}')\rangle, \end{aligned} \quad \text{(A13)}$$

where (h, p) and (h', p') are shorthands of (h_I, p_I) and (h_J, p_J), and $\psi_{h\mathbf{k}}(\mathbf{r})$ is the wave function of a HF band state.

The first term in Eq. (A13) is only nonzero for intraflavor excitations with the h and p (h' and p') states having the same flavor and can be computed in the plane-wave basis. Having $\mathbf{k}+\mathbf{q}+\mathbf{T}_1 = \tilde{\mathbf{k}}$ and $\mathbf{k}'+\mathbf{q}+\mathbf{T}_2 = \tilde{\mathbf{k}}'$ with $\tilde{\mathbf{k}}$ and $\tilde{\mathbf{k}}'$ in the

supercell BZ and $\mathbf{T}_1$ and $\mathbf{T}_2$ the reciprocal lattice vectors of the supercell, this term can be calculated as

$$\langle \psi_{p(\mathbf{k}+\mathbf{q})}\psi_{h'\mathbf{k}'}|V|\psi_{h\mathbf{k}}\psi_{p'(\mathbf{k}'+\mathbf{q})}\rangle = \sum_{\alpha\beta}\sum_{\substack{\mathbf{G}'+\mathbf{Q}'+\mathbf{T}_1\\=\mathbf{G}+\mathbf{Q}+\mathbf{T}_2}} \psi^*_{p\tilde{\mathbf{k}},\alpha\mathbf{G}'}\psi^*_{h'\mathbf{k}',\beta\mathbf{Q}'}\psi_{h\mathbf{k},\alpha\mathbf{G}}\psi_{p'\tilde{\mathbf{k}}',\beta\mathbf{Q}} \times V(\mathbf{k}'+\mathbf{Q}'-\tilde{\mathbf{k}}'-\mathbf{Q}), \tag{A14}$$

where $\psi_{h\mathbf{k}}$ represents the HF state vector in the plane-wave basis. The second term in Eq. (A13) is nonzero for both the intraflavor and interflavor excitations and can be computed as

$$\langle \psi_{p(\mathbf{k}+\mathbf{q})}\psi_{h'\mathbf{k}'}|V|\psi_{p'(\mathbf{k}'+\mathbf{q})}\psi_{h\mathbf{k}}\rangle = \sum_{\alpha\beta}\sum_{\substack{\mathbf{G}'+\mathbf{Q}'+\mathbf{T}_1\\=\mathbf{G}+\mathbf{Q}+\mathbf{T}_2}} \psi^*_{p\tilde{\mathbf{k}},\alpha\mathbf{G}'}\psi^*_{h'\mathbf{k}',\beta\mathbf{Q}'}\psi_{p'\tilde{\mathbf{k}}',\alpha\mathbf{Q}}\psi_{h\mathbf{k},\beta\mathbf{G}} \times V(\mathbf{k}'+\mathbf{Q}'-\mathbf{k}-\mathbf{G}). \tag{A15}$$

With the general density matrix defined as

$$\rho_{\beta\mathbf{Q}',\alpha\mathbf{Q}}(h'\mathbf{k}', p'\tilde{\mathbf{k}}') = \psi^*_{h'\mathbf{k}',\beta\mathbf{Q}'}\psi_{p'\tilde{\mathbf{k}}',\alpha\mathbf{Q}}, \tag{A16}$$

the terms in Eqs. (A14) and (A15) can then be expressed and efficiently calculated as

$$\langle \psi_{p(\mathbf{k}+\mathbf{q})}\psi_{h'\mathbf{k}'}|V|\psi_{h\mathbf{k}}\psi_{p'(\mathbf{k}'+\mathbf{q})}\rangle = \sum_{\alpha\beta}\sum_{\substack{\mathbf{G}'+\mathbf{Q}'+\mathbf{T}_1\\=\mathbf{G}+\mathbf{Q}+\mathbf{T}_2}} \rho^*_{\alpha\mathbf{G},\alpha\mathbf{G}'}(h\mathbf{k}, p\tilde{\mathbf{k}})\rho_{\beta\mathbf{Q}',\beta\mathbf{Q}}(h'\mathbf{k}', p'\tilde{\mathbf{k}}') \times V(\mathbf{k}'+\mathbf{Q}'-\tilde{\mathbf{k}}'-\mathbf{Q}) \tag{A17}$$

and

$$\langle \psi_{p(\mathbf{k}+\mathbf{q})}\psi_{h'\mathbf{k}'}|V|\psi_{p'(\mathbf{k}'+\mathbf{q})}\psi_{h\mathbf{k}}\rangle = \sum_{\alpha\beta}\sum_{\substack{\mathbf{G}'+\mathbf{Q}'+\mathbf{T}_1\\=\mathbf{G}+\mathbf{Q}+\mathbf{T}_2}} \rho^*_{\beta\mathbf{G},\alpha\mathbf{G}'}(h\mathbf{k}, p\tilde{\mathbf{k}})\rho_{\beta\mathbf{Q}',\alpha\mathbf{Q}}(h'\mathbf{k}', p'\tilde{\mathbf{k}}') \times V(\mathbf{k}'+\mathbf{Q}'-\mathbf{k}-\mathbf{G}). \tag{A18}$$

[1] R. Bistritzer and A. H. MacDonald, Moiré bands in twisted double-layer graphene, Proc. Natl. Acad. Sci. USA **108**, 12233 (2011).

[2] E. Suárez Morell, J. D. Correa, P. Vargas, M. Pacheco, and Z. Barticevic, Flat bands in slightly twisted bilayer graphene: Tight-binding calculations, Phys. Rev. B **82**, 121407(R) (2010).

[3] J. M. B. Lopes dos Santos, N. M. R. Peres, and A. H. Castro Neto, Continuum model of the twisted graphene bilayer, Phys. Rev. B **86**, 155449 (2012).

[4] S. Fang and E. Kaxiras, Electronic structure theory of weakly interacting bilayers, Phys. Rev. B **93**, 235153 (2016).

[5] S. Carr, D. Massatt, S. Fang, P. Cazeaux, M. Luskin, and E. Kaxiras, Twistronics: Manipulating the electronic properties of two-dimensional layered structures through their twist angle, Phys. Rev. B **95**, 075420 (2017).

[6] G. Tarnopolsky, A. J. Kruchkov, and A. Vishwanath, Origin of Magic Angles in Twisted Bilayer Graphene, Phys. Rev. Lett. **122**, 106405 (2019).

[7] Y. Ren, Q. Gao, A. H. MacDonald, and Q. Niu, WKB Estimate of Bilayer Graphene's Magic Twist Angles, Phys. Rev. Lett. **126**, 016404 (2021).

[8] Y. Cao, V. Fatemi, A. Demir, S. Fang, S. L. Tomarken, J. Y. Luo, J. D. Sanchez-Yamagishi, K. Watanabe, T. Taniguchi, E. Kaxiras, R. C. Ashoori, and P. Jarillo-Herrero, Correlated insulator behaviour at half-filling in magic-angle graphene superlattices, Nature (London) **556**, 80 (2018).

[9] Y. Cao, V. Fatemi, S. Fang, K. Watanabe, T. Taniguchi, E. Kaxiras, and P. Jarillo-Herrero, Unconventional superconductivity in magic-angle graphene superlattices, Nature (London) **556**, 43 (2018).

[10] K. Kim, A. DaSilva, S. Huang, B. Fallahazad, S. Larentis, T. Taniguchi, K. Watanabe, B. J. LeRoy, A. H. MacDonald, and E. Tutuc, Tunable Moiré bands and strong correlations in small-twist-angle bilayer graphene, Proc. Natl. Acad. Sci. USA **114**, 3364 (2017).

[11] X. Lu, P. Stepanov, W. Yang, M. Xie, M. A. Aamir, I. Das, C. Urgell, K. Watanabe, T. Taniguchi, G. Zhang, A. Bachtold, A. H. MacDonald, and D. K. Efetov, Superconductors, orbital magnets, and correlated states in magic angle bilayer graphene, Nature (London) **574**, 653 (2019).

[12] Y. Xie, B. Lian, B. Jäck, X. Liu, C.-L. Chiu, K. Watanabe, T. Taniguchi, B. A. Bernevig, and A. Yazdani, Spectroscopic signatures of many-body correlations in magic-angle twisted bilayer graphene, Nature (London) **572**, 101 (2019).

[13] A. Kerelsky, L. J. McGilly, D. M. Kennes, L. Xian, M. Yankowitz, S. Chen, K. Watanabe, T. Taniguchi, J. Hone, C. Dean, A. Rubio, and A. N. Pasupathy, Maximized electron interactions at the magic angle in twisted bilayer graphene, Nature (London) **572**, 95 (2019).

[14] Y. Jiang, X. Lai, K. Watanabe, T. Taniguchi, K. Haule, J. Mao, and E. Y. Andrei, Charge order and broken rotational symmetry in magic-angle twisted bilayer graphene, Nature (London) **573**, 91 (2019).

[15] Y. Choi, J. Kemmer, Y. Peng, A. Thomson, H. Arora, R. Polski, Y. Zhang, H. Ren, J. Alicea, G. Refael, F. von Oppen, K. Watanabe, T. Taniguchi, and S. Nadj-Perge, Electronic correlations in twisted bilayer graphene near the magic angle, Nat. Phys. **15**, 1174 (2019).

[16] M. Yankowitz, S. Chen, H. Polshyn, Y. Zhang, K. Watanabe, T. Taniguchi, D. Graf, A. F. Young, and C. R. Dean, Tuning superconductivity in twisted bilayer graphene, Science **363**, 1059 (2019).

[17] A. Uri, S. Grover, Y. Cao, J. A. Crosse, K. Bagani, D. Rodan-Legrain, Y. Myasoedov, K. Watanabe, T. Taniguchi, P. Moon, M. Koshino, P. Jarillo-Herrero, and E. Zeldov, Mapping the twist-angle disorder and landau levels in magic-angle graphene, Nature (London) **581**, 47 (2020).

[18] K. P. Nuckolls, M. Oh, D. Wong, B. Lian, K. Watanabe, T. Taniguchi, B. A. Bernevig, and A. Yazdani, Strongly correlated chern insulators in magic-angle twisted bilayer graphene, Nature (London) **588**, 610 (2020).

[19] D. Wong, K. P. Nuckolls, M. Oh, B. Lian, Y. Xie, S. Jeon, K. Watanabe, T. Taniguchi, B. A. Bernevig, and A. Yazdani,

Cascade of electronic transitions in magic-angle twisted bilayer graphene, Nature (London) **582**, 198 (2020).

[20] U. Zondiner, A. Rozen, D. Rodan-Legrain, Y. Cao, R. Queiroz, T. Taniguchi, K. Watanabe, Y. Oreg, F. von Oppen, A. Stern, E. Berg, P. Jarillo-Herrero, and S. Ilani, Cascade of phase transitions and dirac revivals in magic-angle graphene, Nature (London) **582**, 203 (2020).

[21] Y. Saito, J. Ge, K. Watanabe, T. Taniguchi, and A. F. Young, Independent superconductors and correlated insulators in twisted bilayer graphene, Nat. Phys. **16**, 926 (2020).

[22] P. Stepanov, I. Das, X. Lu, A. Fahimniya, K. Watanabe, T. Taniguchi, F. H. L. Koppens, J. Lischner, L. Levitov, and D. K. Efetov, Untying the insulating and superconducting orders in magic-angle graphene, Nature (London) **583**, 375 (2020).

[23] Y. Luo, R. Engelke, M. Mattheakis, M. Tamagnone, S. Carr, K. Watanabe, T. Taniguchi, E. Kaxiras, P. Kim, and W. L. Wilson, In situ nanoscale imaging of moiré superlattices in twisted van der Waals heterostructures, Nat. Commun. **11**, 4209 (2020).

[24] A. Rozen, J. M. Park, U. Zondiner, Y. Cao, D. Rodan-Legrain, T. Taniguchi, K. Watanabe, Y. Oreg, A. Stern, E. Berg, P. Jarillo-Herrero, and S. Ilani, Entropic evidence for a pomeranchuk effect in magic-angle graphene, Nature (London) **592**, 214 (2021).

[25] N. C. H. Hesp, I. Torre, D. Rodan-Legrain, P. Novelli, Y. Cao, S. Carr, S. Fang, P. Stepanov, D. Barcons-Ruiz, H. Herzig Sheinfux, K. Watanabe, T. Taniguchi, D. K. Efetov, E. Kaxiras, P. Jarillo-Herrero, M. Polini, and F. H. L. Koppens, Observation of interband collective excitations in twisted bilayer graphene, Nat. Phys. **17**, 1162 (2021).

[26] C. Ma, S. Yuan, P. Cheung, K. Watanabe, T. Taniguchi, F. Zhang, and F. Xia, Intelligent infrared sensing enabled by tunable moiré quantum geometry, Nature (London) **604**, 266 (2022).

[27] S. Carr, S. Fang, and E. Kaxiras, Electronic-structure methods for twisted moiré layers, Nat. Rev. Mater. **5**, 748 (2020).

[28] E. Y. Andrei and A. H. MacDonald, Graphene bilayers with a twist, Nat. Mater. **19**, 1265 (2020).

[29] E. Y. Andrei, D. K. Efetov, P. Jarillo-Herrero, A. H. MacDonald, K. F. Mak, T. Senthil, E. Tutuc, A. Yazdani, and A. F. Young, The marvels of moiré materials, Nat. Rev. Mater. **6**, 201 (2021).

[30] J. Liu and X. Dai, Orbital magnetic states in moiré graphene systems, Nat. Rev. Phys. **3**, 367 (2021).

[31] H. C. Po, L. Zou, A. Vishwanath, and T. Senthil, Origin of Mott Insulating Behavior and Superconductivity in Twisted Bilayer Graphene, Phys. Rev. X **8**, 031089 (2018).

[32] M. Koshino, N. F. Q. Yuan, T. Koretsune, M. Ochi, K. Kuroki, and L. Fu, Maximally Localized Wannier Orbitals and the Extended Hubbard Model for Twisted Bilayer Graphene, Phys. Rev. X **8**, 031087 (2018).

[33] J. Kang and O. Vafek, Symmetry, Maximally Localized Wannier States, and a Low-Energy Model for Twisted Bilayer Graphene Narrow Bands, Phys. Rev. X **8**, 031088 (2018).

[34] H. Isobe, N. F. Q. Yuan, and L. Fu, Unconventional Superconductivity and Density Waves in Twisted Bilayer Graphene, Phys. Rev. X **8**, 041041 (2018).

[35] C.-C. Liu, L.-D. Zhang, W.-Q. Chen, and F. Yang, Chiral Spin Density Wave and $d+id$ Superconductivity in the Magic-Angle-Twisted Bilayer Graphene, Phys. Rev. Lett. **121**, 217001 (2018).

[36] J. Kang and O. Vafek, Strong Coupling Phases of Partially Filled Twisted Bilayer Graphene Narrow Bands, Phys. Rev. Lett. **122**, 246401 (2019).

[37] Y.-H. Zhang and T. Senthil, Bridging Hubbard model physics and quantum Hall physics in trilayer graphene/$h-$BN moiré superlattice, Phys. Rev. B **99**, 205150 (2019).

[38] B. L. Chittari, G. Chen, Y. Zhang, F. Wang, and J. Jung, Gate-Tunable Topological Flat Bands in Trilayer Graphene Boron-Nitride Moiré Superlattices, Phys. Rev. Lett. **122**, 016401 (2019).

[39] Y.-H. Zhang, D. Mao, and T. Senthil, Twisted bilayer graphene aligned with hexagonal boron nitride: Anomalous Hall effect and a lattice model, Phys. Rev. Res. **1**, 033126 (2019).

[40] C. Repellin, Z. Dong, Y.-H. Zhang, and T. Senthil, Ferromagnetism in Narrow Bands of Moiré Superlattices, Phys. Rev. Lett. **124**, 187601 (2020).

[41] M. Xie and A. H. MacDonald, Nature of the Correlated Insulator States in Twisted Bilayer Graphene, Phys. Rev. Lett. **124**, 097601 (2020).

[42] N. Bultinck, E. Khalaf, S. Liu, S. Chatterjee, A. Vishwanath, and M. P. Zaletel, Ground State and Hidden Symmetry of Magic-Angle Graphene at Even Integer Filling, Phys. Rev. X **10**, 031034 (2020).

[43] N. Bultinck, S. Chatterjee, and M. P. Zaletel, Mechanism for Anomalous Hall Ferromagnetism in Twisted Bilayer Graphene, Phys. Rev. Lett. **124**, 166601 (2020).

[44] Y. Zhang, K. Jiang, Z. Wang, and F. Zhang, Correlated insulating phases of twisted bilayer graphene at commensurate filling fractions: A Hartree-Fock study, Phys. Rev. B **102**, 035136 (2020).

[45] J. Kang and O. Vafek, Non-Abelian Dirac node braiding and near-degeneracy of correlated phases at odd integer filling in magic-angle twisted bilayer graphene, Phys. Rev. B **102**, 035161 (2020).

[46] F. Wu and S. Das Sarma, Collective Excitations of Quantum Anomalous Hall Ferromagnets in Twisted Bilayer Graphene, Phys. Rev. Lett. **124**, 046403 (2020).

[47] J. Liu and X. Dai, Theories for the correlated insulating states and quantum anomalous Hall effect phenomena in twisted bilayer graphene, Phys. Rev. B **103**, 035427 (2021).

[48] K. Hejazi, X. Chen, and L. Balents, Hybrid Wannier Chern bands in magic angle twisted bilayer graphene and the quantized anomalous Hall effect, Phys. Rev. Res. **3**, 013242 (2021).

[49] S. Liu, E. Khalaf, J. Y. Lee, and A. Vishwanath, Nematic topological semimetal and insulator in magic-angle bilayer graphene at charge neutrality, Phys. Rev. Res. **3**, 013033 (2021).

[50] Y. D. Liao, J. Kang, C. N. Breiø, X. Y. Xu, H.-Q. Wu, B. M. Andersen, R. M. Fernandes, and Z. Y. Meng, Correlation-Induced Insulating Topological Phases at Charge Neutrality in Twisted Bilayer Graphene, Phys. Rev. X **11**, 011014 (2021).

[51] X. Lin and J. Ni, Symmetry breaking in the double moiré superlattices of relaxed twisted bilayer graphene on hexagonal boron nitride, Phys. Rev. B **102**, 035441 (2020).

[52] B. A. Bernevig, Z.-D. Song, N. Regnault, and B. Lian, Twisted bilayer graphene. III. Interacting Hamiltonian and exact symmetries, Phys. Rev. B **103**, 205413 (2021).

[53] B. Lian, Z.-D. Song, N. Regnault, D. K. Efetov, A. Yazdani, and B. A. Bernevig, Twisted bilayer graphene. IV. Exact insulator ground states and phase diagram, Phys. Rev. B **103**, 205414 (2021).

[54] B. A. Bernevig, B. Lian, A. Cowsik, F. Xie, N. Regnault, and Z.-D. Song, Twisted bilayer graphene. V. Exact analytic many-body excitations in Coulomb Hamiltonians: Charge gap, Goldstone modes, and absence of Cooper pairing, Phys. Rev. B **103**, 205415 (2021).

[55] Y. H. Kwan, G. Wagner, T. Soejima, M. P. Zaletel, S. H. Simon, S. A. Parameswaran, and N. Bultinck, Kekulé Spiral Order at All Nonzero Integer Fillings in Twisted Bilayer Graphene, Phys. Rev. X **11**, 041063 (2021).

[56] T. Cea, P. A. Pantaleón, and F. Guinea, Band structure of twisted bilayer graphene on hexagonal boron nitride, Phys. Rev. B **102**, 155136 (2020).

[57] X. Lin, K. Su, and J. Ni, Misalignment instability in magic-angle twisted bilayer graphene on hexagonal boron nitride, 2D Mater. **8**, 025025 (2021).

[58] J. Shi, J. Zhu, and A. H. MacDonald, Moiré commensurability and the quantum anomalous Hall effect in twisted bilayer graphene on hexagonal boron nitride, Phys. Rev. B **103**, 075122 (2021).

[59] D. Mao and T. Senthil, Quasiperiodicity, band topology, and moiré graphene, Phys. Rev. B **103**, 115110 (2021).

[60] J. Shin, Y. Park, B. L. Chittari, J.-H. Sun, and J. Jung, Electron-hole asymmetry and band gaps of commensurate double moire patterns in twisted bilayer graphene on hexagonal boron nitride, Phys. Rev. B **103**, 075423 (2021).

[61] M. Long, P. A. Pantaleón, Z. Zhan, F. Guinea, J. Á. Silva-Guillén, and S. Yuan, An atomistic approach for the structural and electronic properties of twisted bilayer graphene-boron nitride heterostructures, npj Comput. Mater. **8**, 73 (2022).

[62] M. Serlin, C. L. Tschirhart, H. Polshyn, Y. Zhang, J. Zhu, K. Watanabe, T. Taniguchi, L. Balents, and A. F. Young, Intrinsic quantized anomalous Hall effect in a moiré heterostructure, Science **367**, 900 (2020).

[63] C. L. Tschirhart, M. Serlin, H. Polshyn, A. Shragai, Z. Xia, J. Zhu, Y. Zhang, K. Watanabe, T. Taniguchi, M. E. Huber, and A. F. Young, Imaging orbital ferromagnetism in a moiré chern insulator, Science **372**, 1323 (2021).

[64] J. Yu, B. A. Foutty, Z. Han, M. E. Barber, Y. Schattner, K. Watanabe, T. Taniguchi, P. Phillips, Z.-X. Shen, S. A. Kivelson, and B. E. Feldman, Correlated Hofstadter spectrum and flavour phase diagram in magic-angle twisted bilayer graphene, Nat. Phys. **18**, 825 (2022).

[65] E. Khalaf, N. Bultinck, A. Vishwanath, and M. P. Zaletel, Soft modes in magic angle twisted bilayer graphene, arXiv:2009.14827.

[66] A. Kumar, M. Xie, and A. H. MacDonald, Lattice collective modes from a continuum model of magic-angle twisted bilayer graphene, Phys. Rev. B **104**, 035119 (2021).

[67] Y. H. Kwan, Y. Hu, S. H. Simon, and S. A. Parameswaran, Exciton Band Topology in Spontaneous Quantum Anomalous Hall Insulators: Applications to Twisted Bilayer Graphene, Phys. Rev. Lett. **126**, 137601 (2021).

[68] See Supplemental Material at http://link.aps.org/supplemental/10.1103/PhysRevB.107.195434 for figures showing the single-particle and HF band structures in the active-band approximation (Figs. S1 and S2), the full HF band structures (Fig. S3), and the band gaps and the corresponding excitation gaps from full HF calculations (Fig. S4) of TBG/BN with $\theta' = 1.64^\circ$, 0.54°, and -0.56°, and tables listing the large H^0 elements in the plane-wave basis for the pristine TBG and TBG/BN with different θ' (Tables SI–SV).

[69] O. Vafek and J. Kang, Renormalization Group Study of Hidden Symmetry in Twisted Bilayer Graphene with Coulomb Interactions, Phys. Rev. Lett. **125**, 257602 (2020).

[70] J. Kang, B. A. Bernevig, and O. Vafek, Cascades between Light and Heavy Fermions in the Normal State of Magic-Angle Twisted Bilayer Graphene, Phys. Rev. Lett. **127**, 266402 (2021).

[71] J. P. Perdew and A. Zunger, Self-interaction correction to density-functional approximations for many-electron systems, Phys. Rev. B **23**, 5048 (1981).